Performance evaluation of biomass chemical looping gasification in a fluidized bed reactor using industrial waste as oxygen carrier

Goel, Avishek; Panitz, Fabiola; Moghaddam, Elyas M.; Ströhle, Jochen; Epple, Bernd; He, Chao; Konttinen, Jukka

DOI
10.1016/j.biortech.2025.132447

Publication date
2025

Document Version
Final published version

Published in
Bioresource Technology

Bioresource Technology 427 (2025) 132447

Contents lists available at ScienceDirect

Bioresource Technology

journal homepage: www.elsevier.com/locate/biortech

Performance evaluation of biomass chemical looping gasification in a fluidized bed reactor using industrial waste as oxygen carrier

Avishek Goel [a,*], Fabiola Panitz [b], Elyas M. Moghaddam [c], Jochen Ströhle [b], Bernd Epple [b], Chao He [a], Jukka Konttinen [a]

[a] Materials Science and Environmental Engineering, Faculty of Engineering and Natural Sciences, Tampere University, Korkeakoulunkatu 7 Kampusareena, 33720 Tampere, Finland
[b] Technical University of Darmstadt, Department of Mechanical Engineering, Institute for Energy Systems and Technology, Darmstadt, Germany
[c] Faculty of Mechanical Engineering, Process and Energy Department, Delft University of Technology, Netherlands

HIGHLIGHTS

- CLG examined using nickel smelter slag as oxygen carrier in fluidized bed reactor.
- Steam addition facilitated greater char conversion and improved CLG performance.
- Optimal CLG performance: 77.9% carbon conversion and 58.7% cold gas efficiency.
- Nickel smelter slag displayed stable reactivity and minimal sintering behavior.
- Nickel smelter slag is a suitable, cost-effective and eco-friendly oxygen carrier.

GRAPHICAL ABSTRACT

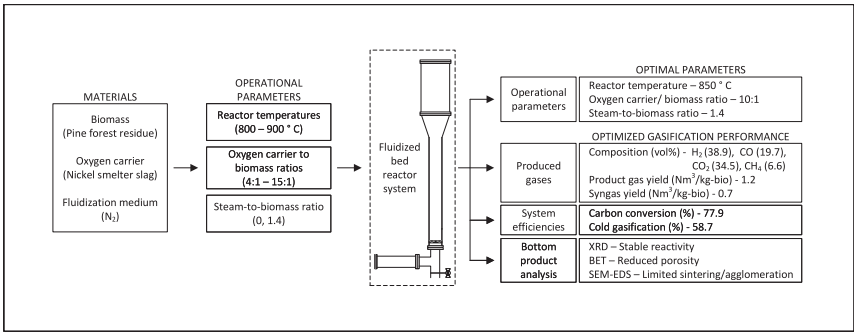

ARTICLE INFO

Keywords:
Chemical looping gasification
Biomass
Industrial waste
Syngas
Fluidized bed

ABSTRACT

The study investigates biomass chemical looping gasification (BCLG) using nickel smelter slag as an oxygen carrier (OC). Key operating parameters, including reactor temperatures (800–900 °C), OC-to-biomass ratio (OCBR, 4:1–15:1), and steam as a gasification medium, were evaluated in a 5kW_{th} fluidized bed reactor using pine forest residue. Performance metrics including gas composition and process efficiencies were assessed. OCs were characterized using XRD, BET and SEM-EDS analyses. Optimal performance was achieved at 850 °C, an OCBR (10:1) and a steam-to-biomass ratio (1.4). The gas composition was 38.87 vol% H_2, 19.65 vol% CO, 34.48 vol% CO_2, and 6.61 vol% CH_4, with a product gas yield of 1.24Nm^3/kg-biomass. Carbon conversion efficiency was 77.85 %, cold gas efficiency 58.70 %, and levelized cost of fuel was 0.15 €/Nm^3 for product gas and 4.55

Abbreviations: a.r., As Received; APC, Annualized Plant Cost; ASU, Air Separation Unit; BCLG, Biomass Chemical Looping Gasification; BCLGO, Biomass Chemical Looping Gasification without steam; BCLGS, Biomass Chemical Looping Gasification with steam; BET, Brunauer-Emmett-Teller; BFB, Bubbling Fluidized Bed Reactor; CCE, Carbon Conversion Efficiency; CCF, Capital Charge Factor; CFB, Circulating Fluidized Bed Reactor; CGE, Cold Gas Efficiency; d.b., Dry Basis; FB, Fluidized Bed; LCOF, Levelized Cost of Fuel; LHV, Lower Heating Value; NS1100, Nickel Smelter Slag calcinated at 1100 °C; OC, Oxygen Carrier; OCBR, Oxygen Carrier to Biomass Ratio; OMCC, Operating and Maintenance Consumables Cost; OMFC, Operating and Maintenance Fixed Cost; PFR, Pine Forest Residue; SBR, Steam to Biomass Ratio; SEM-EDS, Scanning Electron Microscopy with Energy-Dispersive X-Ray Spectroscopy; XRD, X-Ray Diffraction; XRF, X-Ray Fluorescence.

* Corresponding author.
E-mail address: avishek.goel@tuni.fi (A. Goel).

https://doi.org/10.1016/j.biortech.2025.132447
Received 4 September 2024; Received in revised form 14 February 2025; Accepted 23 March 2025
Available online 24 March 2025

€/kg for H_2.The results suggest that steam addition significantly enhanced char conversion, improving overall BCLG efficiency. Moreover, nickel smelter slag demonstrated stability, consistent reactivity, and limited sintering behavior.

1. Introduction

Biomass Chemical Looping Gasification (BCLG) is emerging as a promising technology for converting biomass into syngas due to its economical, efficient and low-emission nature (Goel et al., 2022). BCLG utilizes an oxygen carrier (OC) instead synthetic oxygen and thus eliminates the need for expensive air separation units, which significantly reduces process costs (De et al., 2018). In the case of gasification using air, utilization of OC prevents direct contact of air with the biomass feed, which results in the generation of high-quality N_2-free product gas (Wei et al., 2015). Furthermore, the catalytic properties of the OC facilitate tar cracking, char gasification and reforming, which enhances the process efficiency (Virginie et al., 2012). More importantly, BCLG also possesses inherent CO_2 separation and capture capabilities, which further reduces process emissions (Goel et al., 2022).

Typically, the BCLG process is similar to a dual fluidized bed gasification operation. It involves two interconnected fluidized bed reactors: a fuel reactor and an air reactor. Within the fuel reactor, biomass undergoes partial oxidation using the lattice oxygen provided by OCs, typically metal oxides, that is reduced. Subsequently, in the air reactor, OC is reoxidized by combusting it with air. The reoxidized OC is circulated back to the fuel reactor, thereby conveying oxygen and transferring heat. The understanding of gasification reaction pathways poses significant challenges due to the inherent complexities in the physicochemical properties of biomass. However, a general outline can be conceptualized by understanding the principal reactions that govern the conversion of biomass to product gas. The major reactions involving iron oxide based OC are described below (Wei et al., 2015; Goel et al., 2022).

$$\text{Biomass} \rightarrow \text{Gas}\left(CO, H_2, CO_2, CH_4, C_xH_y\right) + \text{Char} + \text{Ash} + \text{Tar} + H_2O \left(\Delta H > 0\right) \quad \text{(R1)}$$

$$C + CO_2 \leftrightarrow 2CO (\Delta H = +172 MJ/kmol) \quad \text{(R2)}$$

$$C + H_2O \leftrightarrow CO + H_2 \, (\Delta H = +131 MJ/kmol) \quad \text{(R3)}$$

$$CO + H_2O \leftrightarrow CO_2 + H_2 (\Delta H = -41 MJ/kmol) \quad \text{(R4)}$$

$$CH_4 + H_2O \leftrightarrow CO + 3H_2 (\Delta H = +206 MJ/kmol) \quad \text{(R5)}$$

$$CO + 3Fe_2O_3 \rightarrow 2Fe_3O_4 + CO_2 (\Delta H = -47 MJ/kmol) \quad \text{(R6)}$$

$$H_2 + 3Fe_2O_3 \rightarrow 2Fe_3O_4 + H_2O \, (\Delta H = -6 MJ/kmol) \quad \text{(R7)}$$

$$CH_4 + 12Fe_2O_3 \rightarrow 8Fe_3O_4 + CO_2 + 2H_2O \, (\Delta H = +142 MJ/kmol \quad \text{(R8)}$$

In the advancement of BCLG, the investigation of OCs plays a critical role, as it dictates the process performance and economic viability. Generally, an optimal OC should exhibit good reactivity alongside reasonable sintering and abrasion resistance (Deng et al., 2019; Marx et al., 2021). It is equally important that the OC material is available at a low cost, as the lifetime of OC particles is often shortened due to deactivation from biomass ash and potential losses during ash separation from bed material (Hildor et al., 2020). Despite numerous studies on BCLG behavior, the focus has predominantly been on costly OC materials, ranging from synthetic to natural ores to pure metal oxides (e.g., Cu/Ba/Ni/Co– Fe_2O_4, Fe-Cu oxide, Fe_2O_3-CaO, ilmenite, NiO-Fe ore, Mn-Fe ore, Fe- and Cu- ores, and pure Fe_2O_3) (Fan et al., 2020; Hu et al., 2020; Huang et al., 2016; Huang et al., 2014; Wang et al., 2020; Huang et al., 2013; Lin et al., 2020; Chen et al., 2019; Shen et al., 2018; Guo et al., 2015; Condori et al., 2021; Condori et al., 2023; Condori et al., 2021). The investigations utilizing waste materials (e.g., copper slag, LD slag, red mud and sewage sludge ash) remain scarce (Deng et al., 2019; Hildor et al., 2020; Shen et al., 2021; Xu et al., 2021; Liu et al., 2021; Condori et al., 2021). The necessity for further exploration of waste materials is vital, given their potentially advantageous characteristics of adundant availability and low-cost. Moreover, waste materials exhibit distinct behaviors compared to natural ores, pure metal oxides and synthetic OCs due to their intricate compositions, comprising mixtures of metal oxides, impurities and inert compounds (Goel et al., 2023).

To address the gap, nickel smelter slag, an industrial waste material, was investigated as a prospective OC for the BCLG process. It is a by-product of the nickel smelting process, formed through natural cooling or water quenching of the melt generated during the process. It is estimated that approximately 6 to16 tons of nickel slag gets generated for every ton of nickel manufactured (Goel et al., 2022). Moreover, nickel slag has a global annual production of approximately 16 to 40 million tons, with a utilization rate as low as 10 % (Shen et al., 2021). This material has not been previously studied as an OC, nor has its performance been compared to that of other oxygen carrier materials. The selection of the oxygen carrier (OC) was primarily based on its advantageous characteristics. These include abundant availability (estimated between 16 and 40 million tons), low cost (as a waste material, it is cheaper than pure natural ore or synthetic materials), and reasonable reactivity (suitable oxygen transport capacity of 3.3 %). Additionally, it demonstrates high H_2-selectivity, being 8.7 times more selective than pure iron oxide OC. The material also exhibits desirable strength, with a compressive strength of 25.2 MPa, which exceeds the minimum required strength of 20 MPa to prevent attrition. It has an acceptable sintering behavior, indicated by a high sintering onset temperature of 963 °C. These characteristics were identified through our prior research on the evaluation of low-cost OCs for BCLG (Goel et al., 2023).

The primary objective of this study is to holistically investigate BCLG by examining utilization of the OC derived from industrial waste material (e.g., nickel smelter slag) in BCLG. Subsequently, the study highlights the benefits and limitations of BCLG while discussing potential avenues for advancement. The investigation was conducted in an externally heated fluidized bed reactor at the Technical University of Darmstadt using pine forest residue as feedstock and OC developed from nickel smelter slag. The influence of critical operating parameters including reactor temperatures, oxygen carrier-to-biomass ratio (OCBR) and addition of steam as a gasification medium was examined. The process performance was evaluated in terms of product gas compositions, product and syngas yields, carbon conversion and cold gasification efficiencies. Furthermore, fresh and reacted OC materials were analyzed by conducting crystalline phase composition, pore structure and surface morphology analysis.

2. Experimental section

2.1. Materials and characterization

Pine forest residue (PFR) provided by TU Darmstadt (Germany) was utilized as a renewable solid fuel in the study. The PFR was sourced from forestry operations in Sweden and consists of bark and pine needles. The PFR pellets were milled and seived to achieve a particle size of $\leq$ 2000 µm. The particle size distribution is illustrated in Figure A in supplementary document. Table 1 provides a summary of the principal characteristics of PFR.

Nickel smelter slag, sourced from Boliden (Harjavalta, Finland) was utilized as OC for the study. The OC sample was dried at 105 ± 2 °C for 24 h to eliminate moisture. Subsequently, the dried material was

Table 1
Key characteristics of pine forest residue and nickel smelter slag calcinated at 1100 °C.

Particular	Unit	Value
Pine forest residue		
Proximate and ultimate analysis		
Moisture content	(wt%, a.r.)	4.4
Fixed carbon	(wt%, a.r.)	16.6
Volatiles	(wt%, a.r.)	76.8
Ash	(wt%, a.r.)	2.2
C	(wt%, d.b.)	52.3
H	(wt%, d.b.)	6.2
O	(wt%, d.b.)	40.9
S	(wt%, d.b.)	0.03
N	(wt%, d.b.)	0.5
Cl	(wt%, d.b.)	0.01
Lower Heating Value, LHV	(MJ/kg, d.b.)	19.1
Particle diameter	(μm)	≤2000
Nickel smelter slag calcinated at 1100 °C		
Particle diameter	(μm)	≤560
Bulk density	(kg/m^3)	3457.4 ± 14.7
Minimum fluidization velocity, u_{mf}	(m/s)	0.05
Mechanical strength	(MPa)	25.2 ± 1.5
D50 (median particle size)	(μm)	250
Oxygen transport capacity	(%)	3.3
Elemental composition	Fe (39.4 %)Si (7.6 %)Mg (3.3 %)Ca, Al, K, Na (<2%)	
Major XRD phases	Fe_2O_3, $MgFe_2O_4$	

calcinated in a muffle furnace. The temperature of the furnace was gradually increased from room temperature to 1100 °C and maintained at this temperature for 2 h. Following the thermal treatment, the calcined samples were allowed to naturally cool, before being ground and sieved to a particle size of ≤ 560 μm to keep. This particle size was selected to be similar to that of silica sand bed material, ensuring uniform fluidization. The key characteristics of the calcinated nickel smelter slag are summarized in Table 1 and the particle size distribution is depicted in Figure A in supplementary document. The calcinated nickel smelter slag will henceforth be referred to as NS1100.

Elemental composition of both, fresh and reacted OC samples, was determined using an X-ray fluorescence spectrometer (XRF, Bruker Tornado Plus). Crystal structure analysis was conducted via powder XRD with Cu Kα radiation (40 kV, 40 mA) using a Panalytical Empyrean X-Ray Diffractometer. The diffraction measurements spanned a 2θ range of 10° to 90° at a scanning speed of 0.05°s^{-1}. Surface morphology was examined using scanning electron microscopy equipped with energy-dispersive X-ray spectrometer (SEM-EDS, Jeol JSM-IT500). Additionally, the BET surface area and pore volume were determined via N_2 physisorption using a Micrometrics 2017 Flex 3500 micropore gas adsorption analyzer. Prior to measurement, the samples were degassed under vacuum at 523 K for 10 h.

Silica sand was selected as the inert bed material owing to its favorable mechanical properties and inert behavior during gasification process. The silica sand particles possessed a particle diameter of ≤ 355 μm with median particle size (D50) of 200 μm (refer to particle size distribution in Figure A in supplementary document). It exhibited a bulk density of 2602.8 ± 16.7 kg/m^3. The minimum fluidization velocity was determined to be 0.04 m/s.

2.2. Fluidized bed reactor setup and operation

The experimental study was conducted in a ~ 5kW$_{th}$ fluidized bed reactor located at the Technical University of Darmstadt (Germany) to mimic fuel reactor conditions of BCLG system. The schematic diagram of the reactor setup is shown in Fig. 1. The setup was equipped with a comprehensive control system governing parameters such as gas flow-rates, biomass feedrate, temperatures and pressures. The primary

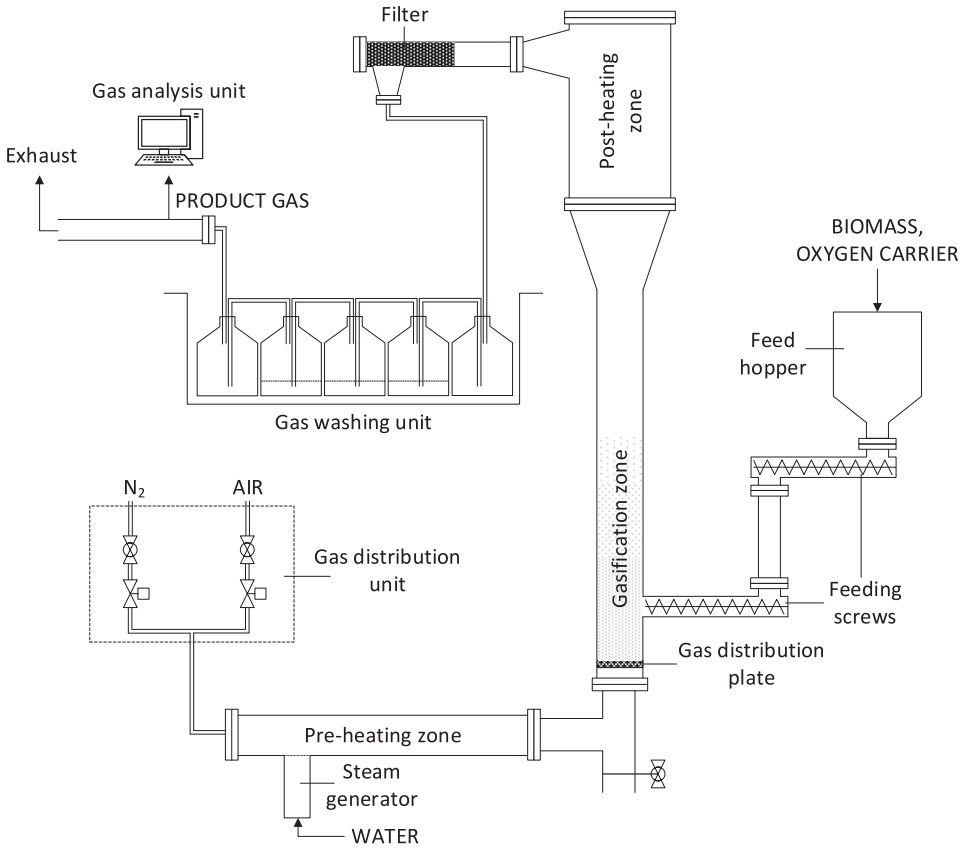

Fig. 1. Schematic diagram of the 5kW$_{th}$ fluidized bed reactor at the Technical University of Darmstadt.

reactor body itself comprised a cylindrical column with an internal diameter of 54.5 mm and a height of 1000 mm. Temperatures and pressures within the reactor were monitored and regulated by sensors positioned at heights of 130 mm, 350 mm and 550 mm from the bottom of the reactor. The reactor body was heated and maintained at the desired temperatures via three electrical heating elements. The gas distribution system governs the control and mixing of gases. A steam generator was utilized to produce superheated steam (~260 °C at atmospheric pressure), which was combined with the gas mixture and passed through a pre-heating zone before being introduced into the reactor through a porous gas distribution plate. The feedstock was continuously supplied from a feed hopper to the reactor using a dual-screw feeding system. The generated gases flow through a post-heating zone, which was externally heated to avert gas condensation. Subsequently, the gases were channeled towards the exhaust system via a filter and a gas washing unit to eliminate impurities and condense tars. A fraction of the produced gas was extracted from the exhaust line and directed towards a continuous gas analysis unit (ABB URAS 206 analyzers) for real-time volumetric gas composition analysis.

Prior to commencing each experiment, PFR and NS1100 were blended in a pre-determined ratio (see Table 2) and the resulting mixture was loaded into the feed hopper. Additionally, the reactor was filled with 2000 g of silica sand, serving as an inert bed material for fluidization. The bottles within the gas washing unit were filled with diesel. To ensure the integrity of the system, a pressure test was conducted to detect any potential leaks. Upon startup, a N_2 stream at a rate of 0.05 Nm^3/h was introduced into the feed hopper to establish an inert atmosphere. Concurrently, another stream of N_2 with the desired flow rate (see Table 2) was introduced into the reactor through the porous gas distribution plate to facilitate inertization and bed material fluidization. Concurrently, the primary reactor body, along with the pre-heating and post-heating zones, was heated to desired temperatures. Throughout the process, temperature and pressure levels were monitored using the installed sensors. Upon reaching targeted temperatures and pressures, the feedstock (along with the blended OC) was introduced into the reactor via the dual-screw feeding system. As necessitated, water was evaporated in the steam generator and subsequently mixed with N_2 before being injected into the reactor. Once a stable composition of produced gas was achieved, the volume fractions of the resultant gases (including CO, CO_2, H_2, and CH_4) were recorded on a dry basis at interval of 5 s. The gas compositions values were averaged for a period of 600 s and reported. At the end of each experiment, the reacted bed material was collected from the bottom of the reactor for evaluation.

In the study, PFR (as received) was gasified using NS1100 as an OC. The operating parameters for every experiment are summarized in Table 2. For each experiment, the biomass feedrate was maintained at a constant level of 1.1 g/min. Multiple experiments were conducted with different OCBR values which ranged between 4:1 and 15:1. The range was selected considering the oxygen transport capacity of NS1100 (c.a. 3.3 %) and corresponds to an equivalence ratio (λ) range of 0.09 to 0.33. The oxygen transport capacity of NS1100 was determined experimentally using H_2-TPR method conducted between 800 and 900 °C. The experiments were conducted at three different reactor temperatures (800, 850 and 900 °C). While investigating BCLG with steam, the steam-to-biomass ratio (SBR) was fixed at 1.4. It is noteworthy that u_f and u_{mf} denote the superficial velocity (m/s) and the minimum fluidization velocity (m/s), respectively.

2.3. Data evaluation

To evaluate the performance of BCLG, various key performance indicators were assessed, including the volumetric composition of product gas, syngas and product gas yields, carbon conversion and cold gas efficiencies.

The volumetric composition of the product gas (CO, H_2, CO_2 and CH_4) was determined by subtracting the volume fraction of N_2 from the total gas composition, with the assumption that the introduced N_2 is inert and not consumed during the process.

$$C_{i_{N2-free}} = \frac{C_i}{100 - \sum_{all} C_i} \tag{1}$$

Where, C_i denotes the dry volume fraction of component i (vol%) recorded by the gas analysis unit.

Since N_2 served as an inert tracer gas, the volumetric flowrate of product gases ($V_{i,out}$, Nm^3/h) was determined by equilibrating N_2 concentrations between inlet and outlet gases, as per the following equation:

$$V_{i,\,out} = C_i \times \frac{V_{N_2,\,in}}{C_{N_2}} \tag{2}$$

where, $V_{N2,in}$ denotes the inlet volume flowrate of N_2 (Nm^3/h) and C_{N2} represents the dry volume fraction of of N_2 (vol%). Additionally, the yield of product gas (Y_{pg}, Nm^3/kg-bio) and syngas (Y_{sg}, Nm^3/kg-bio) was calculated as:

$$Y_{pg} = \frac{V_{H_2,\,out} + V_{CO,out} + V_{CO_2,\,out} + V_{CH_4,\,out}}{m_b} \tag{3}$$

$$Y_{sg} = \frac{V_{H_2,\,out} + V_{CO,out}}{m_b} \tag{4}$$

where, $V_{i,out}$ (Nm^3/h) denotes the volumetric flowrate of individual gas components, respectively.

Moreover, carbon conversion efficiency (CCE, %) is defined as the fraction of carbon of the biomass converted to the valuable syngas components CO, CO_2 and CH_4 and was calculated using the following equation:

$$CCE = \frac{\left(N_{CO,out} + N_{CO_2,\,out} + N_{CH_4,\,out}\right) \times 12}{m_b \times C_{\%}} \times 100 \tag{5}$$

where, N_i (kmol/h) denotes the molar flowrate of individual gas component I, m_b (kg/h) represents the biomass feedrate to the reactor and ($C_{\%}$, wt%) denotes the carbon content present in biomass.

The cold gas efficiency (CGE, %) is defined as the fraction of chemical energy contained in product gas over the total energy of biomass and was calculated as:

Table 2
Experimental matrix for biomass chemical looping gasification.

Parameter	Unit	Value								
Experiment no.	(–)	1	2	3	4	5	6	7	8	9
Reactor temperature	(°C)	800	850	850	850	850	900	800	850	900
Biomass feedrate	(g/min)	1.1	1.1	1.1	1.1	1.1	1.1	1.1	1.1	1.1
OC feedrate	(g/min)	11	4.4	7.7	11	16.5	11	11	11	11
N_2 flowrate	(Nm^3/h)	0.35	0.3	0.3	0.3	0.3	0.3	0.4	0.4	0.4
OCBR	(–)	10:1	4:1	7:1	10:1	15:1	10:1	10:1	10:1	10:1
SBR	(–)	–	–	–	–	–	–	1.4	1.4	1.4
u_f/u_{mf}	(–)	4.1	3.7	3.7	3.4	3.4	3.6	5.5	5.7	5.9
Silica sand	(g)	2000	2000	2000	2000	2000	2000	2000	2000	2000

$$CGE = \frac{LHV_{pg} \times Y_{pg}}{LHV_b} \times 100 \quad (6)$$

where, LHV_{pg} and Y_{pg} denotes the lower heating value (LHV, MJ/Nm^3) and yield of product gas (Nm^3/kg-bio) of the product gas, respectively. LHV_b represents LHV (MJ/kg) of biomass.

2.4. Economic evaluation methodology

An economic evaluation of the BCLG process was conducted to estimate the levelized cost of fuel (LCOF), including the costs for product gas (or H_2). The product gas, can be further processed into various biomass-derived products, such as high-purity H_2, Fischer-Tropsch diesel, biomethanol and bio-olefins. This study, however, does not account for the costs related to upgrading Fischer-Tropsch crude, as the requirements for refining or upgrading vary depending on the final product. The LCOF is influenced by several factors, including the scale of the technology, the underlying economic assumptions, and the estimation methodology. For this analysis, a plant with a capacity of 100 MW_{th} LHV of PFR input was considered. The plant does not have provision for feedstock pretreatment or drying. It is located in Sweden with 2018 as the base year. The plant is assumed to have a 20-year operational lifespan, running 8000 h annually at full capacity. Further details on the cost estimation methodology are presented in Table A1. The LCOF is determined using the equation (7), which calculates the ratio of the total annual costs to the annual production of product gas (or H_2). These annual costs include the sum of the annualized plant cost (APC), operation and maintenance fixed costs (OMFC), and the operation and maintenance costs of consumables (OMCC).

$$LCOF\left(\frac{€}{Nm^3}\right) = \frac{APC + OMFC + OMCC}{AFP} \quad (7)$$

3. Results and discussion

3.1. Typical reactor pressure and temperature

A bubbling fluidized bed reactor was utilized for BCLG investigation. The reactor pressures (*P*1, *P*2 and *P*3) and temperatures (T1, T2 and T3) over the course of the reaction time are illustrated in Figure B in supplementary document. Specifically, *P*1 and T1, *P*2 and T2, and *P*3 and T3 denote the pressures and temperatures at reactor heights of 130 mm, 350 mm and 550 mm, respectively. The average recorded reactor temperatures were 796.8 ± 6.1 °C, 843.1 ± 8.2 °C and 893 ± 12.1 °C, when the temperatures were set to 800 °C, 850 °C and 900 °C, respectively. Generally, the recorded pressures *P*1, *P*2 and *P*3 were 107.8 ± 5.2 mbar, 77.6 ± 5.6 mbar and 23.1 ± 2.2 mbar, respectively. The consistent pressure fluctuations indicate effective fluidization with a well-mixed bed. These observations collectively indicate that the reactor system maintained a stable operational status throughout the experimentation period.

3.2. Effect of reactor temperature

The reactor temperature plays a pivotal role in determining the performance of the BCLG process. It significantly impacts key gasification performance indicators such as gas composition, gas yield, carbon conversion and cold gasification efficiencies. To investigate this influence, the reactor temperature was varied within the range of 800 to 900 °C having a constant OCBR and biomass feedrate of of 10:1 and 1.1 g/min, respectively.

The analysis of dry and N_2-free product gas composition is shown in Fig. 2. Similar composition trends were reported in experimental studies by Wei et al. (Wei et al., 2015) and Ge et al. (Ge et al., 2016). The observed trends can likely be attributed to the complex interplay of endothermic and exothermic reactions, wherein high temperatures, as

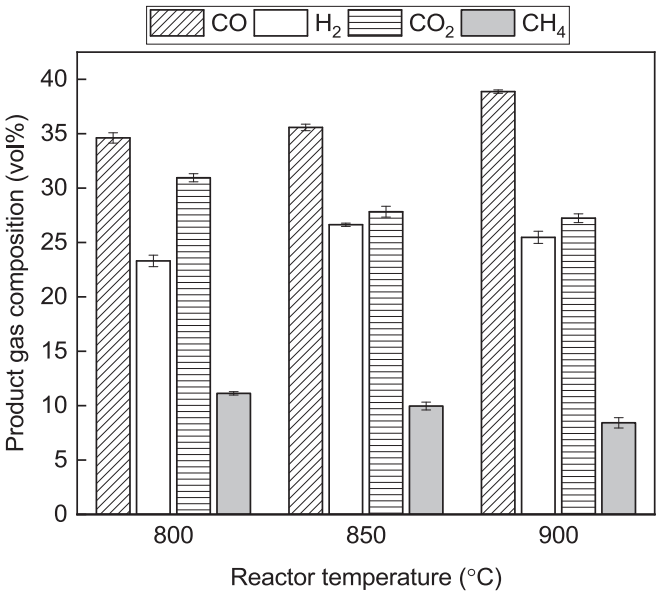

Fig. 2. Effect of reactor temperature on product gas composition at OCBR of 10:1.

dictated by Le Chatelier's principle, facilitate product formation in endothermic reactions and favor reactant formation in exothermic reactions (Nguyen et al., 2021). It is noteworthy that solid–solid interactions are not considered due to their slower kinetics as compared to solid–gas and gas–gas interactions (Wei et al., 2015). However, the residence time of the gases in the reactor was determined to be ~ 5 s, which is considered sufficient for effective gas–solid and gas–gas interactions. This assumption is supported by a study conducted by Rupesh et al. (Rupesh et al., 2022), which investigated the effect of residence time on solid and gaseous reaction species considering a fluidized bed reactor. The results clearly indicate that the product gas composition changes over time and nearly reaches equilibrium at ~ 5 s. Based on Fig. 2, it is observed that the concentration of CO steadily increased from 34.6 to 38.9 (vol%, d.b.) as the reactor temperature increased. This observation aligns with the characteristics of the CO production reactions (R(1) – 3 and R5), which are predominantly endothermic, and the CO consumption reaction (R(4) and R(6), which are exothermic. As the temperature rises, the equilibrium of the endothermic and exothermic reactions shift towards CO production, leading to an increase in CO concentration. The concentration of H_2 exhibited a noteworthy pattern, initially increasing from 23.3 to 26.6 vol% between 800 °C and 850 °C, followed by a decline to 25.5 vol% at 900 °C. H_2 is primarily generated through the endothermic reactions (R(1), *R*3 and R5), which strengthen with increasing temperature. However, the presence of the exothermic oxidation reaction of H_2 with OC (R7) coupled with water–gas shift reaction (R4), resulted in the consumption of H_2 (Nguyen et al., 2021). Additionally, the decline in H_2 concentration at higher temperature (900 °C) suggests that the consumption rate of H_2 oxidation reaction (R7) along with water–gas shift reaction (R4) is higher than the production rate of H_2 (R1, *R*3 and R5). The CO_2 concentration decreased from 31 to 27.2 vol% within the temperature range of 800 – 900 °C. CO_2 is primarily generated during biomass pyrolysis (R1). Additionally, the generation of CO_2 during the oxidation reaction of CO (R6) and CH_4 (R8) with the OC is slow due to the restricted supply of lattice oxygen from the OC (Wei et al., 2015). However, the consumption of CO_2 via both the endothermic boudouard reaction (R2) and the exothermic water–gas reaction (R4) significantly outpaces its production during pyrolysis (R1) and oxidation processes (R6 and R8). Moreover, the limited production of CO_2 during the oxidation processes can be attributed to the restricted lattice oxygen supply by OC (Wei et al., 2015). Consequently, the decline in CO_2 concentration can be

explained by the combined effects of these mechanisms. The CH_4 concentration exhibited a decrease from 11.1 to 8.4 vol% between 800 – 900 °C. The CH_4 in the product gas is primarily contributed from the biomass pyrolysis (R1). However, the steam-methane reforming (R5) and oxidation reaction (R8) consumed the produced CH_4. These reactions act to counterbalance the effect of pyrolysis reaction (R1), which resulted in the reduction of CH_4 with the increased temperature. Moreover, the H_2/CO ratio (not shown in the figure) increased from 0.67 to 0.75 as the temperature increased from 800 to 850 °C, before dropping to 0.66 at 900 °C. This fluctuation is consistent with the changes in gas composition previouslydiscussed.

Fig. 3 illustrates the variations in product gas yield, syngas yield, CCE and CGE. Notably, all the aforementioned gasification performance indicators increased with higher reactor temperature. This phenomenon can be elucidated by the augmentation of endothermic reactions (R(1) – 3 and R5) with increased reactor temperature, which facilitated greater conversion of carbonaceous feedstock into product gas (Wei et al., 2015; Li et al., 2009). Additionally, the concentrations of combustible gases escalated at elevated temperatures. Overall, the best results within the considered range were observed at 900 °C, which can be attributed to the highest gas yields and efficiencies.

3.3. Effect of oxygen carrier to biomass ratio

In the BCLG experiment, NS1100 served as a crucial oxygen source facilitating the conversion of PFR into syngas. However, a higher content of oxygen within the carrier could lead to complete oxidation of biomass into CO_2 and H_2O. Since the desired outcome is syngas rather than heat, maintaining an optimal OCBR (weight ratio of OC to biomass feed) is imperative to prevent excessive oxidation. To determine the optimal OCBR, investigation was conducted across a range from 4:1 to 15:1 at fixed reactor temperature of 850 °C and constant biomass feedrate of 1.1 g/min.

Fig. 4 illustrates the variation of product gas composition across the studied OCBR range. Observing the graph, it becomes evident that the concentrations of H_2, CO and CH_4 decreased, while the CO_2 concentration significantly increased with the increase in OCBR. These trends suggest a shift towards enhanced oxidation reactions facilitated by higher OCBR values, which aligns with the findings reported by Ge et al. (Ge et al., 2016; Ge et al., 2016). Despite the generation of H_2, CH_4, and CO during biomass pyrolysis (R1), water–gas (R2), steam-methane reforming (R5), water–gas shift (R4) and boudouard (R2) reactions,

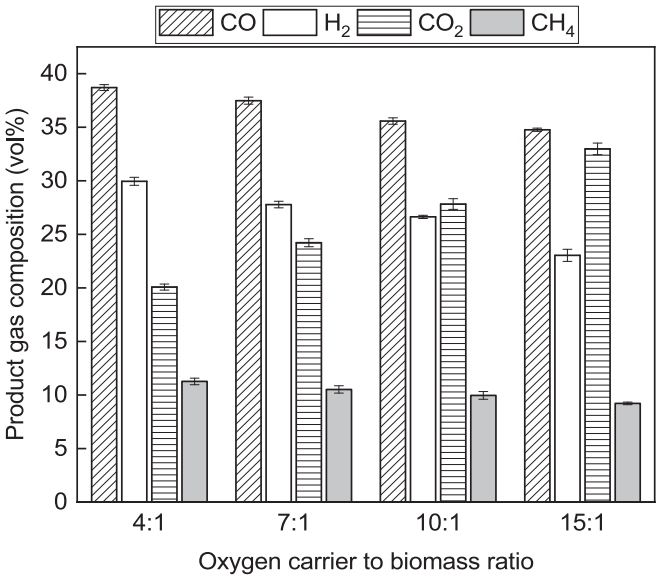

Fig. 4. Effect of OCBR on product gas composition at reactor temperature of 850 °C.

the availability of additional lattice oxygen with higher OCBR intensified oxidation reactions (R(6) – 8). Additionally, the H_2/CO ratio (not shown in the figure) decreased from 0.77 to 0.66 as the OCBR increased. This variation can be attributed to the trend in gas composition discussed before.

To further evaluate the effect of OCBR, Fig. 5 presents the effects of product gas yield, syngas yield, CCE and CGE. Similar trends have been reported by Huang et al. (Huang et al., 2013) and Wei et al. (Wei et al., 2015). With the increase in OCBR, product gas yield and CCE increased. This phenomenon is attributed to the increased intensity of oxidation reactions (R(6) – 8), which consumed gaseous products generated by water–gas reaction (R3). Consequently, this accelerated water–gas reaction (R3), which led to greater conversion of carbon into gaseous products, thereby increasing CCE and product gas yield. Conversely, a contrary trend is observed for syngas yield and CGE, as their values decreased with increasing OCBR. The trend can be attributed to the declining concentrations of CO, H_2 and CH_4 with increasing OCBR,

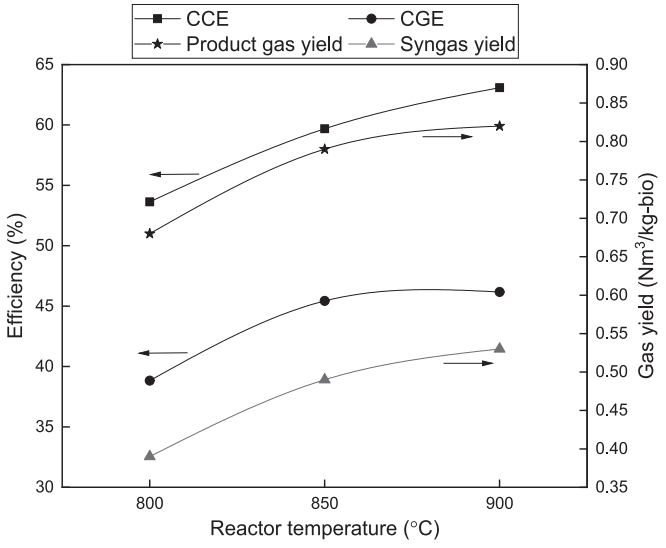

Fig. 3. Effect of reactor temperature on product gas yield, syngas yield, CCE and CGE at OCBR of 10:1.

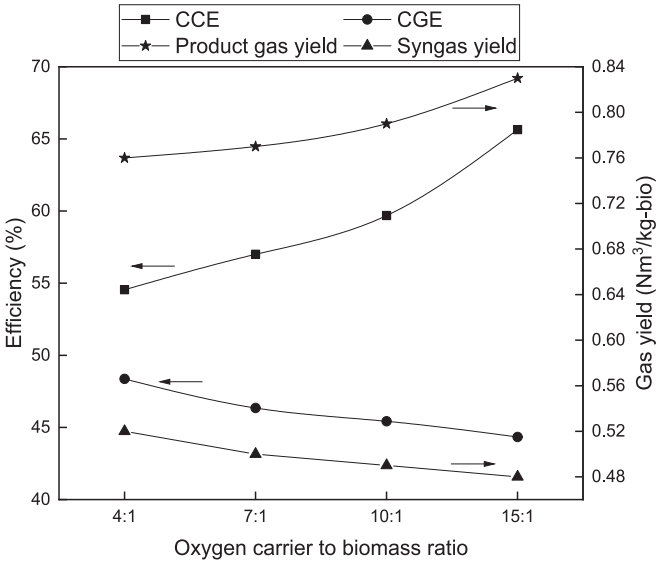

Fig. 5. Effect of OCBR on syngas yield, product gas yield, CCE and CGE at reactor temperature of 850 °C.

resulting from intensified oxidation reactions (R(6) – 8). As CGE depends on the chemical energy of CO, H_2 and CH_4, decreasing concentrations of these gases inevitably led to a reduction in CGE.

Based on the analysis conducted, it can be concluded that an OCBR of 10:1 emerged as the optimal value within the studied range. This conclusion is supported by the balanced product gas composition (see Fig. 4), high product gas and syngas yields and elevated CCE and CGE (refer to Fig. 5). The results suggest that an OCBR of 10:1 provides an optimal balance between PFR feed and NS1100 content, leading to efficient gasification and favorable syngas composition.

3.4. Effect of steam addition as a gasification medium

Steam, recognized for its potential as an oxygen source can play a pivotal role in accelerating the BCLG process. In the experimental investigation, a constant supply of steam (1.5 g/min) blended with N_2 was introduced into the bottom of the reactor, and served as a gasification medium. PFR was continuously fed into the reactor at a rate of 1.07 g/min, mixed with NS1100, maintaining an OCBR of 10:1. The study investigated the effect of steam addition across three different reactor temperatures (i.e., 800, 850 and 900 °C).

The impact of steam addition on the product gas composition across three different reactor temperatures is illustrated in Fig. 6. Regardless of the temperature considered, a consistent trend emerged wherein the concentrations of CO and CH_4 decreased while those of H_2 and CO_2 increased in comparison to without steam. Notably, similar trends have been reported by Ge et al. (Ge et al., 2016) and Zeng et al. (Zeng et al., 2016). Particularly, the concentration of H_2 exhibited a sharp increase, primarily attributed to the water–gas shift reaction (R4), where the addition of steam facilitated the progression of the equilibrium towards the product side. Furthermore, steam addition facilitated H_2 production through water–gas (*R*3) and steam-methane reforming (R5), which also favored the product side. Interestingly, the introduction of steam led to the re-oxidation of the reduced NS1100, as indicated by XRD analysis of the reacted OC (see Fig. 7), which resulted in additional H_2 generation (Huang et al., 2016). Despite steam addition strengthening water–gas and steam-methane reforming reactions (R(3) and R(5), which led to increased CO generation, the consumption of CO during the water–gas shift reaction (R4) outweighed its production. This resulted in a net decrease in CO concentration. The decrease in CO_2 concentration can similarly be explained by the progression of the water–gas shift reaction (R4) towards the product side. The decrease in CH_4 concentration can be attributed to the enhanced steam-methane reforming (R5) under steam-rich conditions.

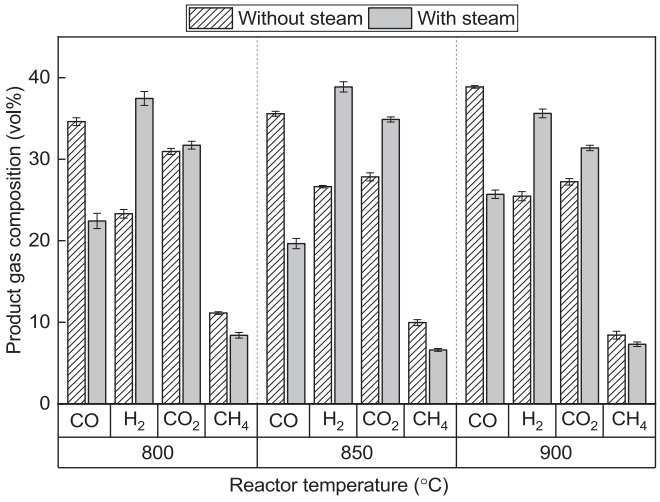

Fig. 6. Effect of steam addition on product gas composition at reactor temperatures of 800 °C, 850 °C and 900 °C.

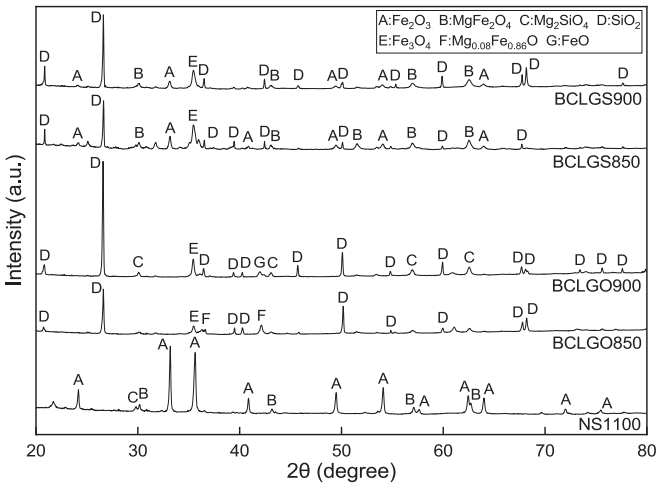

Fig. 7. XRD spectra of fresh and reacted OC samples under different gasification conditions. Here, 'BCLGO' and 'BCLGS' correspond to biomass chemical looping gasification without steam and with steam, respectively. The numerical suffixes 850 and 900 indicate the corresponding reactor temperatures.

Another interesting observation arises concerning reactor temperatures under steam-rich conditions (see Fig. 6). The concentrations of H_2 and CO_2 initially increased and then decreased with increasing reactor temperatures, peaking at 850 °C, while the CH_4 concentration remained relatively stable. Conversely, CO concentration first decreased and then increased, reaching its lowest value at 850 °C. Typically, in the water–gas shift process (R4), the operating temperature and steam addition exerts opposite effects: steam addition tends to drive the reaction towards the product side, while an increase in temperature pushes the reaction towards the reactant side due to its exothermic nature (Babatabar and Saidi, 2021). Consequently, the fluctuations observed in H_2, CO and CO_2 concentrations can be understood by considering the combined impact of these phenomena. Taking into account the variations in gas compositions, the H_2/CO ratio under steam conditions (not shown in the figure) rose from 1.7 to 2.0 as the temperature reached 850 °C, then declined to 1.39 at 900 °C.

To gain further insight into the impact of steam addition as a gasification medium, product gas yield, syngas yield, CCE and CGE were examined for the three reactor temperatures. The results are presented in Table 3. Across all three temperatures, these performance indicators exhibited an increase compared to the gasification method where no additional steam was utilized. The increase in product gas yield and CCE can be attributed to the promotion of water–gas reaction (R3), which resulted in a greater conversion of carbon (char) into gaseous products. Regarding syngas yield and CGE, although the concentrations of CO and CH_4 decreased with steam addition, the sharp increase in H_2 concentration (see Fig. 6) compensated for the yield and chemical energy loss. Consequently, this led to an increased syngas yield and CGE.

In summary, the addition of steam as a gasification medium significantly enhanced key gasification performance indicators including product gas composition (see Fig. 6), syngas and product gas yields, CCE and CGE (refer to Table 3). Within the steam-rich environment, a reactor temperature of 850 °C emerged as the optimal value. This conclusion is supported by the observation of the highest concentration of H_2 and improved gas yields and efficiencies at 850 °C. More importantly, the rate of increment for all performance indicators displayed a more gradual trend beyond 850 °C, which implied a saturation point in gasification performance.

3.5. Analysis of fresh, reacted and regenerated oxygen carrier samples

Structural and surface morphology analyses were conducted on fresh, reacted, and regenerated oxygen carrier samples to understand

Table 3
Effect of steam addition on product gas yield, syngas yield, carbon conversion and cold gas efficiencies at reactor temperatures of 800 °C, 850 °C and 900 °C.

Parameter	Unit	Value					
Reactor temperature	(°C)	800		850		900	
Gasification medium		Without steam	With steam	Without steam	With steam	Without steam	With steam
Product gas yield	Nm^3/kg-bio	0.68	0.92	0.79	1.24	0.82	1.26
Syngas yield	Nm^3/kg-bio	0.39	0.55	0.49	0.72	0.53	0.78
CCE	(%)	53.64	59.06	59.69	77.85	63.09	83.71
CGE	(%)	38.83	47.60	45.43	58.70	46.17	64.37

their reactivity and stability. The reacted sample was regenerated by combusting the reacted sample with air in a separate micro-reactor (CATLAB, Hiden Analytical, UK) at 1000 °C under atmospheric pressure. Analyses of the fresh, regenerated and reacted oxygen carrier samples were performed under various gasification conditions, such as BCLGO850, BCLGO900, BCLGS850 and BCLGS900. Here, 'BCLGO' refers to biomass chemical looping gasification without steam, while 'BCLGS' refers to biomass chemical looping gasification with steam. The numerical suffixes 850 and 900 indicate the corresponding reactor temperatures during the gasification process.

3.5.1. Structural analysis

XRD analysis was conducted to examine the crystalline phase compositions of fresh, reacted and regenerated OC samples under different gasification conditions. The XRD spectra of fresh OC, regenerated and reacted OC samples under various gasification conditions (i.e. BCLGO850, BCLGO900, BCLGS850 and BCLGS900) are illustrated in Fig. 7. The findings offer insights into the structural transformations occurring within the OC material during the BCLG process and provide crucial insights for optimizing BCLG performance.

The structural analysis of fresh OC revealed the presence of two major phases, Fe_2O_3 and $MgFe_2O_4$, along with minor amounts of Mg_2SiO_4. However, in the reacted OC samples, a total of seven crystalline phases were detected: Fe_2O_3, $MgFe_2O_4$, Mg_2SiO_4, SiO_2, Fe_3O_4, $Mg_{0.08}Fe_{0.86}O$, and FeO). Notably, SiO_2 exhibited the highest composition in all reduced NS1100 samples due to the utilization of silica sand as the bed material for fluidization. The reacted OC sample under BCLGO850 and BCLGO900 conditions predominantly consisted of the Fe_3O_4 phase, attributed to CO, H_2 and CH_4 oxidation reactions (R(6) – 8). Additionally, $MgFe_2O_4$ is reduced to $Mg_{0.08}Fe_{0.86}O$, as evidenced by its presence in the reacted OC sample of BCLGO850. Moreover, the presence of FeO in small quantity suggested uneven Fe_2O_3 reduction reactions possibly due to aggregative fluidization characteristics. This behavior aligns with research findings by Huang et al. (Huang et al., 2013; Huang et al., 2014). XRD analysis of reacted OC samples under BCLGS850 and BCLGS900 conditions displayed only Fe_3O_4 and $Mg_{0.08}Fe_{0.86}O$ phases, which indicates no deep reduction. Additionally, the spectra detected their oxidized phases (e.g., Fe_2O_3 and $MgFe_2O_4$), which are attributed to steam providing additional oxygen for reoxidizing the reduced OC and preventing deep reduction. This behavior is consistent with the results presented by Huang et al. (Huang et al., 2016).

More importantly, the analysis of the XRD pattern for the regenerated OC samples (see Figure C in supplementary document) revealed the presence of Fe_2O_3, $MgFe_2O_4$ and SiO_2 phases and is similar to the composition of the fresh OC sample. The observation suggests that the gasification process did not induce any significant alterations in the physical crystal structure of the OC. The presence of these phases indicates successful regeneration of the OC sample and highlights its stable reactivity.

3.5.2. Pore structure analysis

The specific surface area and total pore volume of reacted NS1100 samples under various gasification conditions, such as BCLGO850, BCLGO900, BCLGS850 and BCLGS900, are detailed in Table 4. Across both gasification methods (i.e., BCLGO and BCLGS), it was observed that the specific surface area and total pore volume decreased with increasing reactor temperature. This phenomenon can be attributed to thermal sintering, which promotes the agglomeration of individual OC grains and deposition of biomass ash blocking the pore (Wei et al., 2015; Deng et al., 2019; Huang et al., 2016; Huang et al., 2017). It can be evidenced by the agglomerates present in the reacted OC sample (see Figure D in supplementary document). The specific surface area and total pore volume decreased when steam was added as a gasification medium. This decrease may be ascribed to the accelerated agglomeration tendency of alkali (e.g., K and Na) compounds under a steam-rich environment (Zhao, 2021). Moreover, the addition of steam promoted the formation of alkali silicates and alkali hydroxides, consequently reducing their melting temperatures and enhancing wettability (Zhao, 2021).

The porosity of OC materials is a critical factor influencing their reactivity, with a general observation that reduction in porosity leads to reduced reactivity (Zheng et al., 2022). Contrary to expections, despite the low specific surface area of reacted OC materials, which further decreased with increased reactor temperatures, their reactivity remained stable. The observation is supported by XRD analysis of regenerated OC samples (see Figure C in supplementary document), which highlight structural similarity between regenerated and fresh OC samples, indicating preserved reactivity. Additionally, the consistent reactivity can be explained by the nucleation and nuclei growth process, suggesting that the release of lattice oxygen is not individually affected by the surface structure of the particles (Huang et al., 2017; Hossain and de Lasa, 2010).

3.5.3. Surface morphology analysis

The shape and morphological characteristics of fresh OC sample and reacted OC agglomerates are illustrated in Fig. 8 (magnification 50x), with corresponding EDX spectra presented in Figure E (magnification 1000x) in supplementary document. Analysis of the images revealed, that the smaller particles of fresh OC samples merged together to form a large particle during the gasification process and resulted in agglomerated structures in the reacted OC samples. Moreover, the formation of agglomerates can be attributed to the presence of alkalis (K and Na) as indicated by the EDX spectra of the reacted OC samples (see Figure E in supplementary document). The presence of K and Na under reducing atmospheres promote agglomeration due to formation of less thermally

Table 4
Pore structure analysis of the reacted oxygen carrier sample under different gasification conditions. Here, 'BCLGO' and 'BCLGS' denotes biomass chemical looping gasification conducted without steam and with steam, respectively. The numerical suffixes 850 and 900 signify the corresponding reactor temperatures.

Sample	Surface area (m^2/g)	Total pore volume (cm^3/g)
BCLGO850	1.412	0.0015
BCLGO900	0.467	0.0007
BCLGS850	0.837	0.0011
BCLGS900	0.261	0.0004

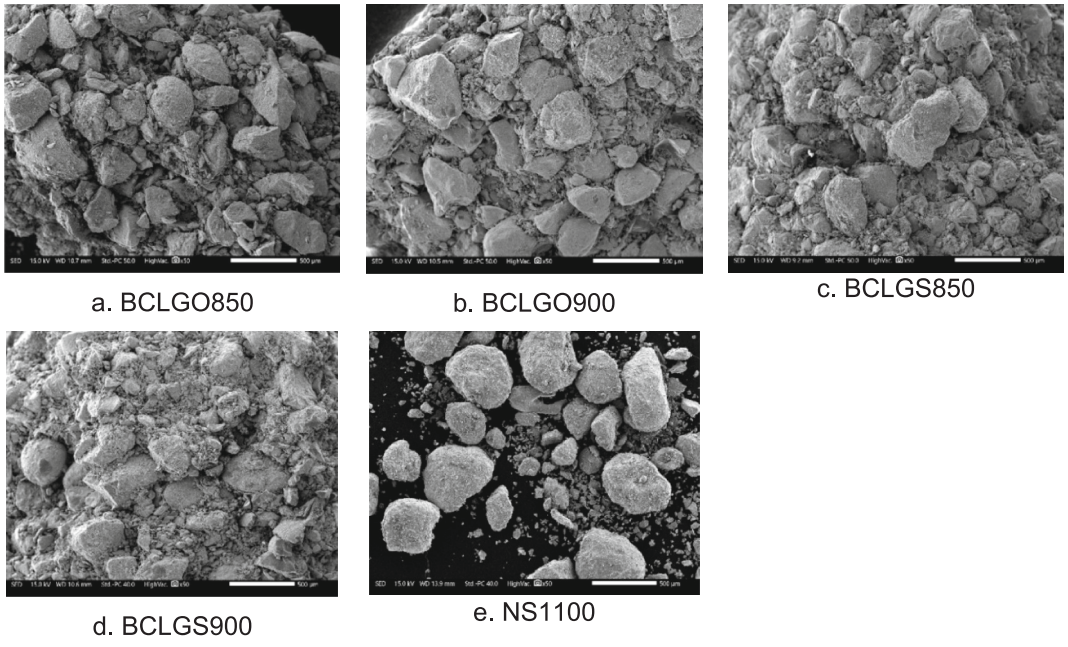

Fig. 8. SEM images (magnification 50x) of reacted OC agglomerates and fresh OC samples under different gasification conditions. Figure a-d represents reacted OC samples and figure e respresents fresh OC sample. Here, 'BCLGO' and 'BCLGS' correspond to biomass chemical looping gasification without steam and with steam, respectively. The numerical suffixes 850 and 900 indicate the corresponding reactor temperatures.

stable silicates (Goel et al., 2023; Zhao, 2021). Additionally, the presence of S, Na and Cr, in addition to Mg, Al, Si, K and Ca, on the surface of reacted OC samples suggests deposition of biomass ash.

Further examination of the SEM images (Figure E in supplmentary document, maginification 1000x) revealed that the fresh OC sample possesses a porous structure with its surface loosely covered by smaller OC granules. Additionally, the reacted OC sample under BCLGO850 conditions exhibit good porosity due to its open structure. However, a reduction in open pore structure is observed in the reacted samples under BCLGS850 conditions, followed by a more pronounced reduction in the BCLGO900 and BCLGS900 OC samples. The trend aligns with the BET results, which indicate that increased reactor temperatures and the addition of steam lead to decreased porosity.

3.6. Comparative gasification performance analysis of nickel smelter slag against pure and synthetic oxygen carriers

The performance comparison of nickel smelter slag as an OC in BCLG process was conducted against other categories of OCs, including pure and synthetic type. Key gasification performance indicators of the present study was compared against existing BCLG studies (Wei et al., 2015; Guo et al., 2015; Condori et al., 2021; Huang et al., 2014; Wei et al., 2015). The comparison results are presented in Table 5. It should be noted that the studies compared have similar operating conditions with operating temperature ranging between 650 and 940 °C. These studies employed pine as their biomass feedstock. The table compares the gasification results of industrial waste (e.g., nickel smelter slag) from the current study to pure and synthetic materials (e.g., iron and copper ore, ilmenite, Fe_2O_3/Al_2O_3 and $Fe_2O_3.NiO/Al_2O_3$).

The H_2 concentration in the present study is higher compared to the studies using Fe_2O_3/Al_2O_3 (Wei et al., 2015) and $Fe_2O_3.NiO/Al_2O_3$ (Wei et al., 2015) as oxygen carriers. The CGE in the present study are similar to the results reported for Fe_2O_3/Al_2O_3 as an oxygen carrier. However, the CGE results are inferior compared to those using $Fe_2O_3.NiO/Al_2O_3$. Additionally, in the present study, the CCE is lower compared to the other two studies. One of the contributing factor is the use of interconnected fluidized bed reactors, which extend the interaction time between OC particles with biomass char and volatiles. Additionally, the Fe_2O_3/Al_2O_3 and $Fe_2O_3.NiO/Al_2O_3$ OCs are composed of pure materials, containing ~ 70 wt% Fe_2O_3 in contrast to 39.4 wt% of Fe present in its oxide form in NS1100. Moreover, the inclusion of NiO further improved the reactivity of the OC due to higher reactivity than Fe_2O_3 (Goel et al., 2022). Although the material cost of the mentioned synthetic OCs is significantly higher than that of nickel smelter slag. Additionally, both studies reported limited sintering, similar to the findings in the present study.

When comparing the gasification performance of the present study to that using copper ore as the oxygen carrier (Guo et al., 2015), all

Table 5
Comparison of results from different biomas chemical looping gasification studies. Here, FB refers to fluidized bed.

Reactor type	Oxygen carrier	Operational temperature (°C)	H_2 (vol%)	CO (vol%)	CCE (%)	CGE (%)	Ref. research
$5kW_{th}$-FB	Nickel smelter slag	800–900	23–38.9	19.6–38.7	53.6–83.7	38.8–64.4	Present study
$10kW_{th}$ inter-FB	Fe_2O_3/Al_2O_3	675–900	8–25	38–44	84–94	42–61	(Wei et al., 2015)
FB	Copper ore	800	14	17	83.2	26.6	(Guo et al., 2015)
FB	Iron ore	767–927	22–27	49–53	75–85	69–84	(Huang et al., 2014)
$10kW_{th}$-FB	$Fe_2O_3.NiO/Al_2O_3$	760–910	18–27.5	29–47	71.2–97.8	64.4–84.5	(Wei et al., 2015)
$1.5KW_{th}$ inter FB	Ilmenite	820–940	18.4–39.9	13.5–35.7	88.4–97.5	54–92.9	(Condori et al., 2021)

performance indicators, including H_2 and CO concentrations, CCE, and CGE, are superior. The inferior performance with copper ore can be attributed to the reduction reaction of CuO, which consumes some of the produced syngas to generate heat. Thus, inexpensive nickel smelter slag proves to be a better OC option for BCLG compared to the more expensive copper ore. Additionally, slight sintering was observed in both studies.

In the experimental study using iron ore as an oxygen carrier (Huang et al., 2014), the H_2 concentration is lower than in the present study. The CO concentration showed similar performance between the two studies. The lower CCE observed in the present study can be linked to the lower concentration of 39.4 wt% Fe (in the form of iron oxide) in NS1100 compared to 91 wt% of Fe_2O_3 in the iron ore. This higher concentration of Fe_2O_3 results in greater reactivity, which in turn contributes to the increased CCE when iron ore is used as OC. However, the CGE is observed to be better when using iron ore as OC. Notably, the authors reported issues related to defluidization due to the deep reduction of iron ore to FeO, leading to agglomeration during reoxidation. In contrast, the present study did not encounter any issues related to deep reduction and defluidization.

In an experimental study using ilmenite as an oxygen carrier (Condori et al., 2021), the H_2 and CO concentrations were similar to those observed in the present study. However, the lower CCE and CGE in this study can be attributed to the lower iron oxide content in NS1100 (39.4 wt% Fe) compared to ilmenite, which contains higher amounts of iron oxides in the form of Fe_2TiO_5 (57.4 wt%) and Fe_2O_3 (11 wt%). The higher iron oxide content in ilmenite increases reactivity, leading to higher efficiencies. Additionally, the use of interconnected fluidized bed reactors in the previous study may have contributed to the increased efficiencies by extending the interaction time between the oxygen carrier, biomass char and volatiles.

Comparing the H_2 concentration among all the studies, it can be noted that NS1100 offers higher H_2 concentration (indicating, a higher H_2/CO ratio). This can be attributed to the high H_2-selectivity of nickel smelter slag, as highlighted by Goel et al. (Goel et al., 2023). The authors displayed that nickel smelter slag exhibited controlled oxidation of CH_4; thereby offering strong selectivity toward partial oxidation. Altogether, it can be said the utilization of industrial waste-derived OC, such as nickel smelter slag, yielded gasification performances similar to or even better than that of expensive pure or synthetic OCs. Thus, nickel smelter slag offers a cost-effective, environmentally friendly and readily available alternative for achieving high BCLG performance.

3.7. Economic analysis

The plant cost estimation takes into account the expenses associated with the gasification island, which includes systems such as the fuel handling unit, BCLG reactor setup and flue gas unit. In particular, it includes lock hoppers, bubbling fluidized bed (BFB) and circulating fluidized bed (CFB) reactors, refractories, condensate treatment, steam generator, cooler, filter, fan and ash handling system. The cost estimates for the BCLG reactor system are derived from economic data of the GoBiGas plant, a bio-methane facility that utilizes a dual-fluidized bed gasification system with both BFB and CFB reactors (Thunman et al., 2018; Roshan Kumar et al., 2022). The plant cost estimation follows the methodology outlined in Table A1.

The results of BCLG economic evaluation are presented in Table 6. The annualized plant cost was determined using a capital charge factor (CCF) to distribute the plant cost over the plant's operational lifetime. For a plant in Sweden with an assumed 20-year lifespan, the CCF is estimated to be approximately 10.4 % per year (Roshan Kumar et al., 2022). The annual OMFC cover both labor and maintenance expenses, while the annual OMCC account for the costs of the oxygen carrier material, process water, and PFR. Detailed calculations are provided in Table A2. The estimates for annual production of product gas and H_2 were derived from experimental data, as shown in Table A2. Here it should be noted that the results from the current BCLG experiments using semi-continous unit have been scaled up to provide a reasonable estimate of the gas production and its associated costs. The LCOF for both product gas and H_2 was calculated using equation (7).

Table 6
Economic evaluation of biomass chemical looping gasification. Here PG refers to product gas.

Particular	Unit	Cost
Plant cost	M€/year	42.55
Annualized plant cost	M€/year	4.43
Annual operation and maintenace fixed cost	M€/year	9.52
Annual operation and maintenace consumables cost	M€/year	14.58
Annual total cost	M€/year	28.53
Product gas production	Nm^3/year	1.95×10^8
H_2 production	Nm^3/year	7.6×10^7
$LCOF_{PG}$	€/Nm^3	0.15
$LCOF_{H2}$	€/Nm^3 / €/kg	0.38 / 4.55

The LCOF for product gas and H_2 generation for BCLG was calculated to be 0.15 €/Nm^3 and 4.55 €/kg, respectively. Parkinson et al. (Parkinson et al., 2019) reported H_2 production costs for various technologies: steam methane reforming (€1-2/kg), coal gasification (€1.8–2.2/kg), biomass gasification (€1.5–3/kg), electrolysis powered by wind (€3.9–9.3/kg), solar (€6.6–13.8/kg) and nuclear (€4.6–7.0/kg). When comparing these costs, it is evident that H_2 production via BCLG is less expensive than electrolysis but more expensive than steam methane reforming and coal or biomass gasification. However, it should be noted that the H_2 production costs in this study are based on raw product gas. Incorporating reforming adjustment units downstream of the BCLG process, along with dual-fluidized bed systems that enable longer residence times and higher efficiency, could improve H_2 production and further reduce costs. More importantly, the current analysis considered nickel smelter slag at €30 per ton (Rydén et al., 2018), which is significantly cheaper than synthetic oxygen carriers like CO_3O_4/Al_2O_3 (€27,500 per ton (Aghabararnejad et al., 2015) and Fe_2O_3 + Mn_2O_3/CuO (€19,200 per ton (Fleiß et al., 2024). Using the current LCOF calculation methodology, the utilization of these expensive synthetic oxygen carriers could increase H_2 production costs by approximately 80–85 %.

3.8. Perspectives on advancement of biomass chemical looping gasification

In summary, the findings of the study indicate that BCLG offers an effective solution to efficiently convert biomass into syngas. This innovative approach has demonstrated the production of high-quality syngas with optimal product gas compositions, high gas yields and system efficiencies. Additionally, the utilization of calcinated nickel smelter slag as an oxygen carrier material has shown fair reactivity, stable reaction performance and controlled sintering behavior, which affirms its suitability. However, the study has highlighted challenges associated with agglomeration of OC material. It was observed that higher reactor temperatures and utilization of steam as a gasification medium promoted thermal sintering of OC material. The phenomenon leads to a loss in porosity and the formation of agglomerates, necessitating further research to mitigate sintering. A potential solution to avoid agglomeration could be the introduction of inert support/binder materials such as Al_2O_3 or TiO_2 and natural clays like bentonite (Breault, 2018). Additionally, as discussed by Zhao (Zhao, 2021), agglomeration may be mitigated by using various bed additives (e.g., Al/Si−, Ca−, Pa − or S − based compounds) to prevent the formation of low-melting point alkali (K and Na) compounds. Furthermore, discussion by Breault (Breault, 2018) about use of a spouted fluidized bed system featuring cyclic and vigorous solid-particle movement may potentially prevent bed agglomeration.

The study did not consider different sizes of OC particles and was

conducted using particles with a mean size (D50) of 250 μm. However, investigating the influence of OC particle size on gasification performance is crucial since particle size directly affects reaction rates considering the small residence time in the reactor. Therefore, optimizing the particle size can further improve the system efficiencies by achieving sufficient oxidation conversions.

The findings suggested that the OC achieved stable performance and reactivity. However, it is important to note that the experiments were conducted using a lab-scale (~5kW_{th}) bubbling fluidized reactor with fresh OC material for each set. These tests subjected the particles to less stress compared to a circulating fluidized bed reactor system. Therefore, it is crucial to investigate the performance of nickel smelter slag material in a larger-scale (e.g. pilot scale) circulating fluidized bed reactor system to better understand its attrition behavior and test the cyclability and lifespan of the OC material.

The study was conducted using an allothermal bubbling fluidized bed reactor. During each experiment, reduced OC material got accumulated as the bottom product as it could only be removed at the end. A potential avenue for further investigation involves exploring the use of an autothermal dual fluidized bed reactor system, which would examine heat and mass transfer management (via OC material) between the two reactors. Furthermore, the accumulation of reduced OC material may have affected reactivity rates. Therefore, investigating systems that allow for the replacing of poisoned OC material with fresh material is crucial, as it could impact process performance. Under such conditions, the OCBR may vary due to considerations of both heat and mass transfer and the periodic recharging of OC material.

The study did not explore the effect of residence time on the interaction between OC particles and produced volatiles and gases. In the current bubbling fluidized bed reactor system, the residence time is brief (c.a. ~ 5 s). Therefore, it is essential to investigate the residence time distribution of OC particles, preferably using a circulating fluidized bed system. Optimizing the residence time, could significantly improve operational efficiency and impact reactor design.

4. Conclusion

Biomass Chemical Looping Gasification of pine forest residue was conducted in an allothermal fluidized bed reactor using nickel smelter slag as the oxygen carrier (OC). Adding steam significantly improved the performance by enhancing gas yields and efficiencies, due to improved char conversion. Optimal gasification conditions were found to be 850 °C (reactor temperature), 10:1 (OC-to-biomass ratio) and 1.4 (steam-to-biomass ratio). Under these conditions, high-quality product gas with H_2, CO, CO_2, and CH_4 concentrations of 38.9 vol%, 19.7 vol%, 34.5 vol% and 6.6 vol%, respectively, was achieved. Product and syngas yields were 1.24 Nm^3/kg-bio and 0.72 Nm^3/kg-bio, with CCE and CGE of 77.85 % and 58.70 %. Structural analysis of nickel smelter slag displayed consistent and stable reactivity, despite a reduction in specific surface area, suggesting nucleation and nuclei growth process for lattice oxygen supply. The samples demonstrated no significant reduction and structural changes and exhibited limited sintering and agglomeration, even with biomass ash deposition. Moreover, its comparison against pure and synthetic OCs displayed similar or even superior gasification performance. Furthermore, the levelized cost of H_2 production was calculated at 4.55 €/kg, which is 80–85 % cheaper than using synthetic OCs. Overall, nickel smelter slag offers a cost-effective, eco-friendly and readily available alternative.

CRediT authorship contribution statement

Avishek Goel: Conceptualization, Data curation, Formal analysis, Investigation, Methodology, Funding acquisition, Visualization, Project administration, Writing – original draft. **Fabiola Panitz:** Methodology, Resources, Writing – review & editing. **Elyas M. Moghaddam:** Writing – review & editing, Methodology. **Jochen Ströhle:** Methodology, Resources, Writing – review & editing. **Bernd Epple:** Resources, Writing – review & editing. **Chao He:** Conceptualization, Methodology, Project administration, Resources, Supervision, Visualization, Writing – review & editing. **Jukka Konttinen:** Conceptualization, Methodology, Resources, Supervision, Funding acquisition, Project administration, Validation, Visualization, Writing – review & editing.

Declaration of competing interest

The authors declare the following financial interests/personal relationships which may be considered as potential competing interests: Avishek Goel reports travel was provided by Climate Neutral Energy Systems and Society. Avishek Goel reports equipment, drugs, or supplies was provided by Technical University of Darmstadt. Chao He reports financial support was provided by Research Council of Finland. If there are other authors, they declare that they have no known competing financial interests or personal relationships that could have appeared to influence the work reported in this paper.

Acknowledgement

This work is supported by Tampere University (Finland), Climate Neutral Energy Systems and Society (Finland) and the Technical University of Darmstadt (Germany). The authors would like to acknowledge the support of Leo Hyvärinen, Kati Valtonen, Merja Ritola and Turkka Salminen during the characterization of materials. The authors would also like to acknowledge Boliden for providing nickel smelter slag utilized in the study. C. H. acknowledges the Academy Research Fellowship and its related research project funded by Research Council of Finland (decision numbers: 341052, 346578).

Appendix A. Supplementary data

Supplementary data to this article can be found online at https://doi.org/10.1016/j.biortech.2025.132447.

Data availability

Data will be made available on request.

References

Goel, A., Moghaddam, E.M., Liu, W., He, C., Konttinen, J., 2022. Biomass chemical looping gasification for high-quality syngas: A critical review and technological outlooks. Energy Conversion and Management 268, 116020. https://doi.org/10.1016/j.enconman.2022.116020.

De, S., Agarwal, A.K., Moholkar, V., Thallada, B., 2018. Coal and biomass gasification. Energy, Environment, and Sustainability.

Wei, G., He, F., Huang, Z., Zheng, A., Zhao, K., Li, H., 2015. Continuous operation of a 10 kWth chemical looping integrated fluidized bed reactor for gasifying biomass using an iron-based oxygen carrier. Energy Fuels 29, 233–241. https://doi.org/10.1021/ef5021457.

Virginie, M., Adánez, J., Courson, C., De Diego, L., García-Labiano, F., Niznansky, D., Kiennemann, A., Gayán, P., Abad, A., 2012. Effect of Fe–olivine on the tar content during biomass gasification in a dual fluidized bed. Applied Catalysis b: Environmental 121, 214–222.

Deng, Z., Huang, Z., He, F., Zheng, A., Wei, G., Meng, J., Zhao, Z., Li, H., 2019. Evaluation of calcined copper slag as an oxygen carrier for chemical looping gasification of sewage sludge. International Journal of Hydrogen Energy 44, 17823–17834.

Marx, F., Dieringer, P., Ströhle, J., Epple, B., 2021. Design of a 1 MWth pilot plant for chemical looping gasification of biogenic residues. Energies 14, 2581. https://doi.org/10.3390/en14092581.

Hildor, F., Leion, H., Linderholm, C.J., Mattisson, T., 2020. Steel converter slag as an oxygen carrier for chemical-looping gasification. Fuel Processing Technology 210, 106576.

Fan, Y., Tippayawong, N., Wei, G., Huang, Z., Zhao, K., Jiang, L., Zheng, A., Zhao, Z., Li, H., 2020. Minimizing tar formation whilst enhancing syngas production by integrating biomass torrefaction pretreatment with chemical looping gasification. Applied Energy 260, 114315.

Hu, Q., Shen, Y., Chew, J.W., Ge, T., Wang, C.-H., 2020. Chemical looping gasification of biomass with Fe2O3/CaO as the oxygen carrier for hydrogen-enriched syngas production. Chemical Engineering Journal 379, 122346.

Huang, Z., Zhang, Y., Fu, J., Yu, L., Chen, M., Liu, S., He, F., Chen, D., Wei, G., Zhao, K., 2016. Chemical looping gasification of biomass char using iron ore as an oxygen carrier. International Journal of Hydrogen Energy 41, 17871–17883.
Huang, Z., He, F., Feng, Y., Zhao, K., Zheng, A., Chang, S., Wei, G., Zhao, Z., Li, H., 2014. Biomass char direct chemical looping gasification using NiO-modified iron ore as an oxygen carrier. Energy & Fuels 28, 183–191.
Wang, S., Song, T., Yin, S., Hartge, E.-U., Dymala, T., Shen, L., Heinrich, S., Werther, J., 2020. Syngas, tar and char behavior in chemical looping gasification of sawdust pellet in fluidized bed. Fuel 270, 117464.
Huang, Z., Fang, H., Xin-ai, L., Kun, Z., Hai-bin, L., Zeng-li, Z., 2013. Syngas generated by chemical-looping gasification of biomass using Fe2O3 as oxygen carrier in presence of steam. Acta Energy Sol Sin 34, 2056–2062.
Lin, Y., Wang, H., Huang, Z., Liu, M., Wei, G., Zhao, Z., Li, H., Fang, Y., 2020. Chemical looping gasification coupled with steam reforming of biomass using NiFe2O4: Kinetic analysis of DAEM-TI, thermodynamic simulation of OC redox, and a loop test. Chemical Engineering Journal 395, 125046.
Chen, J., Zhao, K., Zhao, Z., He, F., Huang, Z., Wei, G., 2019. Identifying the roles of MFe2O4 (M= Cu, Ba, Ni, and Co) in the chemical looping reforming of char, pyrolysis gas and tar resulting from biomass pyrolysis. International Journal of Hydrogen Energy 44, 4674–4687.
Shen, T., Ge, H., Shen, L., 2018. Characterization of combined Fe-Cu oxides as oxygen carrier in chemical looping gasification of biomass. International Journal of Greenhouse Gas Control 75, 63–73.
Guo, L., Zhao, H., Zheng, C., 2015. Synthesis gas generation by chemical-looping reforming of biomass with natural copper ore as oxygen carrier. Waste and Biomass Valorization 6, 81–89.
Condori, O., de Diego, L.F., Garcia-Labiano, F., Izquierdo, M.T., Abad, A., Adánez, J., 2021. Syngas production in a 1.5 kWth biomass chemical looping gasification unit using Fe and Mn ores as the oxygen carrier. Energy & Fuels 35, 17182–17196.
Condori, O., Abad, A., Izquierdo, M.T., de Diego, L.F., García-Labiano, F., Adánez, J., 2023. Assessment of the chemical looping gasification of wheat straw pellets at the 20 kWth scale. accessed February 7, 2025 Fuel 344, 128059. https://www.sciencedirect.com/science/article/pii/S0016236123006725.
Condori, O., García-Labiano, F., Diego, L.F., Izquierdo, M.T., Abad, A., Adánez, J., 2021. Biomass chemical looping gasification for syngas production using ilmenite as oxygen carrier in a 1.5 kWth unit. Chemical Engineering Journal 405, 126679.
Shen, X., Yan, F., Zhang, Z., Li, C., Zhao, S., Zhang, Z., 2021. Enhanced and environment-friendly chemical looping gasification of crop straw using red mud as a sinter-resistant oxygen carrier. Waste Management 121, 354–364.
Xu, F., Xing, X., Gao, S., Zhang, W., Zhu, L., Wang, Y., Chen, J., Chen, H., Zhu, Y., 2021. Direct chemical looping gasification of pine sawdust using Fe2O3-rich sludge ash as an oxygen carrier: Thermal conversion characteristics, product distributions, and gasification performances. Fuel 304, 121499.
Liu, F., Wu, X., Zhang, X., Yang, L., Liu, Y., Song, Z., 2021. Co-use of organic herbal residue and red mud waste for syngas production by chemical looping gasification. International Journal of Energy Research 45, 2195–2210.
Condori, O., García-Labiano, F., Luis, F., Izquierdo, M.T., Abad, A., Adánez, J., 2021. Biomass chemical looping gasification for syngas production using LD Slag as oxygen carrier in a 1.5 kWth unit. Fuel Processing Technology 222, 106963.
Goel, A., Ismailov, A., Moghaddam, E.M., He, C., Konttinen, J., 2023. Evaluation of low-cost oxygen carriers for biomass chemical looping gasification. Chemical Engineering Journal 469, 143948. https://doi.org/10.1016/j.cej.2023.143948.
Ge, H., Guo, W., Shen, L., Song, T., Xiao, J., 2016. Biomass gasification using chemical looping in a 25 kWth reactor with natural hematite as oxygen carrier. Chemical Engineering Journal 286, 174–183. https://doi.org/10.1016/j.cej.2015.10.092.
Nguyen, N.M., Alobaid, F., Epple, B., 2021. Chemical looping gasification of torrefied woodchips in a bubbling fluidized bed test rig using iron-based oxygen carriers. Renewable Energy 172, 34–45. https://doi.org/10.1016/j.renene.2021.03.006.
Rupesh, S., Muraleedharan, C., Arun, P., 2022. Influence of residence time on syngas composition in CaO enhanced air–steam gasification of biomass. Environ Dev Sustain 24, 8363–8377. https://doi.org/10.1007/s10668-021-01787-1.
Li, C., Hirabayashi, D., Suzuki, K., 2009. Development of new nickel based catalyst for biomass tar steam reforming producing H2-rich syngas. Fuel Processing Technology 90, 790–796. https://doi.org/10.1016/j.fuproc.2009.02.007.
Ge, H., Guo, W., Shen, L., Song, T., Xiao, J., 2016. Experimental investigation on biomass gasification using chemical looping in a batch reactor and a continuous dual reactor. Chemical Engineering Journal 286, 689–700. https://doi.org/10.1016/j.cej.2015.11.008.
Huang, Z., He, F., Feng, Y., Liu, R., Zhao, K., Zheng, A., Chang, S., Zhao, Z., Li, H., 2013. Characteristics of biomass gasification using chemical looping with iron ore as an oxygen carrier. International Journal of Hydrogen Energy 38, 14568–14575. https://doi.org/10.1016/j.ijhydene.2013.09.022.
Zeng, J., Xiao, R., Zeng, D., Zhao, Y., Zhang, H., Shen, D., 2016. High H2/CO ratio syngas production from chemical looping gasification of sawdust in a dual fluidized bed gasifier. Energy & Fuels 30, 1764–1770.
Babatabar, M.A., Saidi, M., 2021. Hydrogen production via integrated configuration of steam gasification process of biomass and water-gas shift reaction: Process simulation and optimization. International Journal of Energy Research 45, 19378–19394. https://doi.org/10.1002/er.7087.
Huang, Z., He, F., Zhao, K., Feng, Y., Zheng, A., Chang, S., Zhao, Z., Li, H., 2014. Natural iron ore as an oxygen carrier for biomass chemical looping gasification in a fluidized bed reactor. Journal of Thermal Analysis and Calorimetry 116, 1315–1324.
Huang, Z., Xu, G., Deng, Z., Zhao, K., He, F., Chen, D., Wei, G., Zheng, A., Zhao, Z., Li, H., 2017. Investigation on gasification performance of sewage sludge using chemical looping gasification with iron ore oxygen carrier. International Journal of Hydrogen Energy 42, 25474–25491.
L. Zhao, Agglomeration during Fluidized Bed Combustion and Gasification of Biomass, (2021).
Zheng, H., Jiang, X., Gao, Y., Tong, A., Zeng, L., 2022. Chemical looping reforming: process fundamentals and oxygen carriers. Discov Chem Eng 2, 5. https://doi.org/10.1007/s43938-022-00012-3.
Hossain, M.M., de Lasa, H.I., 2010. Reduction and oxidation kinetics of Co–Ni/Al2O3 oxygen carrier involved in a chemical-looping combustion cycles. Chemical Engineering Science 65, 98–106. https://doi.org/10.1016/j.ces.2009.01.059.
Wei, G., He, F., Zhao, Z., Huang, Z., Zheng, A., Zhao, K., Li, H., 2015. Performance of Fe–Ni bimetallic oxygen carriers for chemical looping gasification of biomass in a 10 kWth interconnected circulating fluidized bed reactor. International Journal of Hydrogen Energy 40, 16021–16032. https://doi.org/10.1016/j.ijhydene.2015.09.128.
Thunman, H., Seemann, M., Berdugo Vilches, T., Maric, J., Pallares, D., Ström, H., Berndes, G., Knutsson, P., Larsson, A., Breitholtz, C., Santos, O., 2018. Advanced biofuel production via gasification – lessons learned from 200 man-years of research activity with Chalmers' research gasifier and the GoBiGas demonstration plant. Energy Science & Engineering 6, 6–34. https://doi.org/10.1002/ese3.188.
Roshan Kumar, T., Mattisson, T., Rydén, M., 2022. Techno-economic assessment of chemical looping gasification of biomass for Fischer–Tropsch crude production with net-negative CO2 emissions: part 2. Energy Fuels 36, 9706–9718. https://doi.org/10.1021/acs.energyfuels.2c01184.
Parkinson, B., Balcombe, P., Speirs, J., Hawkes, A., Hellgardt, K., 2019. Levelized cost of CO2 mitigation from hydrogen production routes. Energy & Environmental Science 12, 19–40.
Rydén, M., Hanning, M., Lind, F., 2018. Oxygen carrier aided combustion (OCAC) of wood chips in a 12 MWth circulating fluidized bed boiler using steel converter slag as bed material. Applied Sciences 8, 2657. https://doi.org/10.3390/app8122657.
Aghabararnejad, M., Patience, G.S., Chaouki, J., 2015. Techno-Economic Comparison of a 7-MWth Biomass Chemical Looping Gasification Unit with Conventional Systems. Chemical Engineering & Technology 38, 867–878. https://doi.org/10.1002/ceat.201400503.
Fleiß, B., Priscak, J., Hammerschmid, M., Fuchs, J., Müller, S., Hofbauer, H., 2024. CO2 capture costs of chemical looping combustion of biomass: A comparison of natural and synthetic oxygen carrier. Journal of Energy Chemistry 92, 296–310. https://doi.org/10.1016/j.jechem.2024.01.048.
Breault, R.W., 2018. Handbook of chemical looping technology. John Wiley & Sons.